



**Predictions of identification and production of new superheavy nuclei with  $Z = 119$  and 120**G. G. Adamian <sup>1</sup>, N. V. Antonenko,<sup>1,2</sup> H. Lenske <sup>3</sup> and L. A. Malov<sup>1</sup><sup>1</sup>*Joint Institute for Nuclear Research, 141980 Dubna, Russia*<sup>2</sup>*Tomsk Polytechnic University, 634050 Tomsk, Russia*<sup>3</sup>*Institut für Theoretische Physik der Justus-Liebig-Universität, D-35392 Giessen, Germany*

(Received 26 November 2019; accepted 20 February 2020; published 3 March 2020)

Effective single-particle potentials obtained from the established nonrelativistic nuclear energy density functional approach are incorporated into the microscopic-macroscopic method to calculate the ground-state shell corrections, mass excesses, and  $Q_\alpha$  values for heaviest nuclei. The low-lying one-quasiparticle states are studied in the isotonic chains with neutron numbers  $N = 175, 176, \text{ and } 177$ . The isomeric states are discussed in the odd isotopes. The possible  $\alpha$ -decay chains of nuclei  $^{295}119$  and  $^{295,297}120$  are analyzed and compared with the available experimental data. The termination of the  $\alpha$ -decay chains by spontaneous fission is analyzed. The production cross sections are calculated for superheavy nuclei with  $112 \leq Z \leq 120$  in the actinide-based complete fusion reactions with projectiles  $^{48}\text{Ca}$ ,  $^{48,50}\text{Ti}$ ,  $^{54}\text{Cr}$ ,  $^{58}\text{Fe}$ , and  $^{64}\text{Ni}$ .

DOI: [10.1103/PhysRevC.101.034301](https://doi.org/10.1103/PhysRevC.101.034301)**I. INTRODUCTION**

The synthesis and spectroscopic study of superheavy nuclei (SHN) are going well in recent years. The experiments on complete fusion reactions with  $^{48}\text{Ca}$  beam and various actinide targets have been successfully carried out at FLNR (Dubna), GSI (Darmstadt), and LBNL (Berkeley) [1–11] in order to synthesize superheavy nuclei with  $Z = 112\text{--}118$ . The first attempts [12,13] have been made to produce the nuclei with  $Z = 119$  and 120, which are the next elements beyond the known element Og. The investigation of transfermium elements expands our knowledge of the low-lying one-, two-quasiparticle, and collective states, isomers, location of the shell closures, and decay modes [14]. The spectroscopic study of nuclear states is up to date because of the problem of unambiguous identification of new SHN [1,4,15]. For example, the existing microscopic-macroscopic [16–26] and self-consistent [27–51] approaches supply us the basis for the intensive calculations of the properties of SHN.

Studies of production cross sections and structural properties of SHN rely strongly on the predictions of the shell effects for which the single-particle dynamics is the driving force. The microscopic-macroscopic method combines quantal single-particle dynamics with semiclassical collective degrees of freedom covering the macroscopic aspects of a nucleus, as typically replaced by in the liquid-drop picture. The shell effects are incorporated by adding the microscopic spectral information obtained from the phenomenological mean-field potentials. Thus, a good account for the single-particle potential is mandatory to strengthen the predictive power of the model. Because the self-consistent approaches can describe the structural peculiarities, a meaningful extension is to incorporate the self-consistently derived HFB mean-field potentials into the microscopic-macroscopic method. The mean-field potentials obtained from either nonrelativistic Hamiltonian

energy densities or covariant Lagrangian densities are converted into the Schrödinger-equivalent single-particle potentials, appropriate for the microscopic-macroscopic method. These potentials are defined under the constraint that we obtain an equivalent, effective wave equation with the kinetic energy operator containing only a constant mass term in order to comply with the microscopic-macroscopic method. The general scheme for the extraction of the Schrödinger-type mean-field potential from the self-consistent approaches is introduced in Ref. [52].

The aim of the present paper is to apply the microscopic-macroscopic approach [26] with the effective single-particle potentials obtained for the SHN from the self-consistent HFB calculations using the established nonrelativistic nuclear energy density functional (EDF) approach [40], and to reveal the trends in the shell effects, nuclear binding energies,  $Q_\alpha$  values, quasiparticle states, and evaporation residue cross sections of SHN. Of great interest for experimental work is the prediction of isomeric states and  $\alpha$ -decay branchings into higher energy levels. The knowledge of possible spread of the  $\alpha$ -particle energies, the  $\alpha$ -decay half-lives, and the terminations of the  $\alpha$ -decay chains of  $^{295}119$  and  $^{295,297}120$  is important for the experimental identification of these nuclei. Hitherto, all hot fusion reactions for the synthesis of SHN have been performed with the beams of  $^{48}\text{Ca}$ . The new nuclei with  $Z \geq 119$  would be hopefully produced in future experiments using available actinide targets and beams of nuclei heavier than  $^{48}\text{Ca}$ . The comparative analysis of different hot fusion reactions is of great importance for the synthesis of elements 119 and 120. Our goal is to find the favorable reaction partners and the beam energy. The structure of SHN crucially influences the evaporation residue cross sections in the actinide-based hot fusion reactions [68]. With the shell closure at  $Z \geq 120$ , the survival probability of the compound nuclei with  $Z = 119$  and 120 may be much higher. Employing the dinuclear system

fusion approach [53–70] and the predictions of nuclear properties with the microscopic-macroscopic method containing the effective single-particle potentials from the self-consistent HFB approach, we will calculate the production cross sections of nuclei with  $Z = 119$  and 120.

The paper is organized as follows: in Secs. II and III, we introduce the self-consistent nonrelativistic HFB approach [40] with D3Y interaction and the microscopic-macroscopic approach, respectively. Note that the self-consistent approach is used without any readjustment of parameters. We use the mean-field potential obtained with the HFB model in the microscopic-macroscopic model. In this way we can relate these models and reveal the differences. In Sec. IV, the Woods-Saxon (WS) potential from the HFB is used in the microscopic-macroscopic calculations to find the shell corrections, mass excesses,  $Q_\alpha$  values in the ground state of SHN, and one-quasiparticle excitations in nuclei of  $\alpha$ -decay chain of elements  $^{295}_{119}$  and  $^{295,297}_{120}$ . The evaporation residue cross sections are calculated for superheavy nuclei with  $112 \leq Z \leq 120$ . Finally, we summarize our work in Sec. V.

## II. SELF-CONSISTENT HFB APPROACH

The EDF

$$\mathcal{E}(\rho, \tau, \kappa) = \mathcal{E}_{\text{kin}}(\tau) + \mathcal{E}_{\text{int}}(\rho) + \mathcal{E}_{\text{pair}}(\rho, \kappa) - \sum_{q=p,n} \lambda_q \rho_q \quad (1)$$

is given by the kinetic-energy density  $\mathcal{E}_{\text{kin}}$ , the interaction energy density  $\mathcal{E}_{\text{int}}$  and the pairing interaction density  $\mathcal{E}_{\text{pair}}$ . The functional  $\mathcal{E}$  depends on the proton and neutron densities  $\rho = \{\rho_p, \rho_n\}$ , the corresponding kinetic energy densities  $\tau = \{\tau_p, \tau_n\}$ , and the pairing densities  $\kappa = \{\kappa_p, \kappa_n\}$ . In order to enforce particle number conservation, the proton and neutron chemical potentials  $\lambda_{p,n}$  are introduced. The interactions contained in  $\mathcal{E}_{\text{int}}$  and  $\mathcal{E}_{\text{pair}}$  are derived from in-medium  $G$ -matrix interactions, which is supplemented by an effective three-body interaction in order to describe properly the saturation properties of infinite nuclear matter. Following the density matrix expansion scheme [71] as used in Ref. [40], an effective density dependent local two-body interaction is constructed, incorporating already antisymmetrization. Hence, our approach is based effectively on an energy density functional with

$$\mathcal{E}_{\text{kin}}(1, 2) = \sum_{q=p,n} \tau_q(1, 2), \quad (2)$$

$$\begin{aligned} \mathcal{E}_{\text{int}}(1, 2) = & \frac{1}{2}(\rho^\dagger(1)V_{00}(1, 2)\rho(2) + \rho_1^\dagger(1)V_{01}(1, 2)\rho_1(2)) \\ & + \mathcal{E}_C(1, 2) + \mathcal{E}_{s.o.}(1, 2) + \mathcal{E}_{res}(1, 2), \end{aligned} \quad (3)$$

$$\mathcal{E}_{\text{pair}}(1, 2) = \frac{1}{2} \sum_{q=p,n} \kappa_q^\dagger(1)V_{qq}(1, 2)\kappa_q(2), \quad (4)$$

where  $V_{00}$  and  $V_{01}$  denote the interaction form factors in the isoscalar and isovector interaction channels which for spin-saturated nuclear systems have nonzero ground-state expectation values.  $V_{qq}$  indicates the pairing interaction for protons and neutrons, respectively, taken here as the contact interaction with the strength fixed by the singlet-even on-shell

scattering matrix at the local Fermi momentum  $k_q = k_{F_q}(\rho_q)$ . All interaction form factors depend on the density as discussed in Ref. [40]. Residual interactions, which do not contribute to the ground state of a spin-saturated nucleus, are contained in  $\mathcal{E}_{res}$ . In addition, in a finite nucleus also the Coulomb and spin-orbit densities are given in terms of the charge density  $\rho_c$  and the spin-orbit energy density  $\rho_{s.o.}$ :

$$\mathcal{E}_C(1, 2) = \frac{1}{2}e^2\rho_c^\dagger(1)\tilde{V}_C(1, 2)\rho_c(2) \quad (5)$$

$$\mathcal{E}_{s.o.}(1, 2) = \frac{1}{2} \sum_{T=0,1} W_T(1, 2)\mathbf{J}_T^\dagger(1)\nabla\rho_T(2) + \text{H.c.}, \quad (6)$$

where the interaction  $\tilde{V}_C$  accounts for antisymmetrization effects, which we treat in local density approximation with an effective density-dependent contact interaction. The spin-orbit energy density is defined in terms of the isoscalar and isovector interactions  $W_T$  and the corresponding spin currents  $\mathbf{J}_T$ . The isoscalar and isovector densities are given in terms of the proton and neutron ground state as

$$\rho = \rho_n + \rho_p \quad \text{and} \quad \rho_1 = \rho_n - \rho_p, \quad (7)$$

respectively.

The kinetic, nucleon, and pairing densities are defined in terms of single-particle wave functions  $\varphi_{qjm}$  and occupation probabilities  $n_{jm} = v_{jm}^2$  and emptiness  $u_{jm}^2 = 1 - v_{jm}^2$ :

$$\tau_q = \sum_{jm} v_{jm}^2 \frac{\hbar^2}{2m_q} |\nabla\varphi_{qjm}|^2, \quad (8)$$

$$\rho_q = \sum_{jm} v_{jm}^2 |\varphi_{qjm}|^2, \quad (9)$$

$$\kappa_q = \frac{1}{2} \sum_{jm} u_{jm}v_{jm} |\varphi_{qjm}|^2. \quad (10)$$

The isospin spin currents are given by

$$\mathbf{J}_T = \sum_{q,jm} v_{qjm}^2 \varphi_{qjm}^\dagger \tau^T [-i\nabla \times \sigma] \varphi_{qjm}. \quad (11)$$

In a spherical nucleus, only the radial projection  $J_{rT} = \mathbf{r}\mathbf{J}_T$  contributes effectively,

$$J_{rT} = \sum_{q,jm} v_{qjm}^2 \varphi_{qjm}^\dagger \tau^T \ell \cdot \sigma \varphi_{qjm}, \quad (12)$$

which is seen to describe the spin-orbit density. The charge density  $\rho_c(k)$  is obtained by folding the proton and neutron densities (9) by the corresponding proton and neutron charge form factors, respectively, taken from the experiment [72,73].

Variation of  $\mathcal{E}$  with respect to  $\varphi_{qjm}^\dagger$  leads to the equations for the single-particle wave functions

$$\left( -\frac{\hbar^2\nabla^2}{2m_q} + U_q + e_q U_C + U_{ls} \ell \cdot \sigma + \Delta_q - \varepsilon_{qj} \right) \varphi_{qjm} = 0 \quad (13)$$

with the single-particle self-energy

$$U_q = \frac{\delta}{\delta\rho_q} (\mathcal{E}_{\text{int}} + \mathcal{E}_{\text{pair}}), \quad (14)$$

which accounts for isoscalar and isovector contributions and includes rearrangement self-energies due to the intrinsic

density dependence of the interactions [41]. The pairing field is

$$\Delta_q = \frac{\delta}{\delta\kappa_q} \mathcal{E}_{\text{pair}} \sim V_{qq}(\rho_q)\kappa_q, \quad (15)$$

where we neglect higher-order corrections from the variation of the state-dependent gaps, which are defined by the matrix elements  $\Delta_{qj} = \langle qjm|\Delta_q|qjm\rangle$  of the pairing field, and determine the quasiparticle energies and occupation numbers in the BCS approximation. In a spherical nucleus they are independent of the magnetic quantum numbers, and, thus, given as

$$E_{qj} = \sqrt{(\varepsilon_{qj} - \lambda_q)^2 + \Delta_{qj}^2}, \quad (16)$$

$$v_{qj}^2 = \frac{1}{2} \left( 1 - \frac{\varepsilon_{qj} - \lambda_q}{E_{qj}} \right). \quad (17)$$

The parameters entering into Eqs. (13) are defined in Ref. [40].

### III. MICROSCOPIC-MACROSCOPIC APPROACH

The single-particle potentials from HFB calculations are fitted in the WS form [52]

$$U_q(r) = \frac{V_q^0}{1 + \exp[(r - R_q)/a_q]},$$

where  $V_q^0 = -(58.3 \pm 32 \frac{N-Z}{A})$  MeV,  $r_{0N} = 1.24$  fm,  $r_{0Z} = 1.25$  fm,  $a_N = 0.68$  fm,  $a_Z = 0.75$  fm. For the spin-orbit potential, we use the derivative of  $U_q(r)$  with the constants  $\kappa_N = 0.35$  fm<sup>2</sup> and  $\kappa_Z = 0.27$  fm<sup>2</sup>, which are slightly different from those in Ref. [52] and provide a better agreement of shell corrections with previous calculations [18,25] for known nuclei. Though, the parameters of WS potential are extracted from the HFB calculations for the spherical nuclei, they are relevant to consider the nuclear deformation in the microscopic-macroscopic model. The found Woods-Saxon potentials are employed in the microscopic-macroscopic approach [26] to find the shell corrections and the binding energies in the ground states of SHN. We used 27 subshells with the orbital angular momentum  $l = 0-14$  and 26 subshells with  $l = 1-13$  in diagonalization of the WS potential for the states of positive and negative parities, respectively.

The potential energy is calculated as the sum of two terms

$$U = U_{\text{LDM}} + \delta U_{\text{mic}}. \quad (18)$$

The first term is a smoothly varying macroscopic energy (the Coulomb and surface energies) calculated with the liquid-drop model. The second term  $\delta U_{\text{mic}}$  contains the shell  $E_{\text{sh}}$  and pairing corrections arising due to the shell structure of nucleus. The equilibrium deformation of the nucleus corresponds to the position of the minimum on the potential energy surface  $U$ . The calculation of equilibrium deformations is carried out using the basis of the microscopic-macroscopic two-center shell model (TCSM), taking into account the pairing and shell corrections. In the TCSM, two parameters, the length  $\lambda$  of the nucleus and the deformations  $\beta$  of ellipsoid parts, are used to describe the nuclear shape near the ground state. This shape, being expanded in spherical harmonics, contains  $\beta_{20}$ ,  $\beta_{40}$ , and

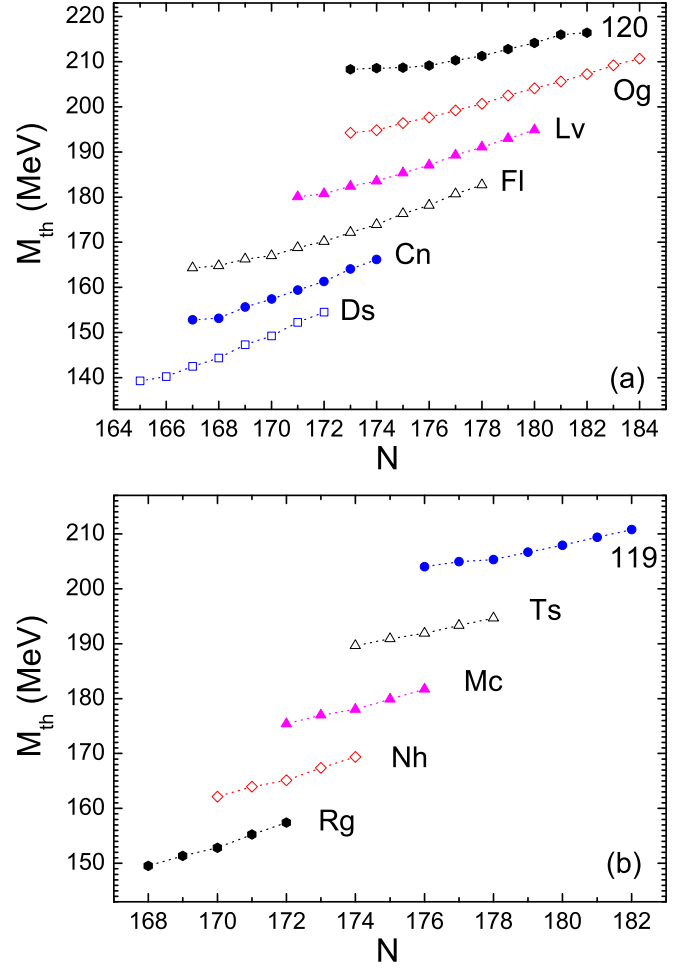


FIG. 1. Calculated mass excesses (symbols connected by lines) for (a) even- $Z$  and (b) odd- $Z$  nuclei with  $110 \leq Z \leq 120$ . The microscopic-macroscopic method is used with the Woods-Saxon potential extracted from the HFB self-consistent consideration.

higher multiplicities. For each  $\lambda$  and  $\beta$ , the lower part of the TCSM spectrum is replaced by the corresponding states of the WS potential at corresponding  $\beta_{20}$  and  $\beta_{40}$ . As shown in Ref. [26], the energy spectra in this WS potential and in the TCSM potential are close. So, our method is clearly suitable only for the ground state because for larger deformations two TCSM parameters are not enough to describe realistic nuclear shape.

For nuclei with  $Z < 110$ , the absolute values of microscopic corrections obtained in our calculations are close to those obtained in Refs. [18,19,23]. As found, the considered isotopes of nuclei with  $Z = 114-120$  are almost spherical, i.e., they have the parameters of quadrupole deformation smaller than 0.15.

## IV. RESULTS OF CALCULATIONS

### A. Properties of heaviest nuclei

#### 1. Mass excesses and $Q_\alpha$ values

The calculated mass excesses  $M_{\text{th}}$  and  $Q_\alpha$ -values are presented in Figs. 1 and 2 for nuclei with  $112 \leq Z \leq 120$ . We

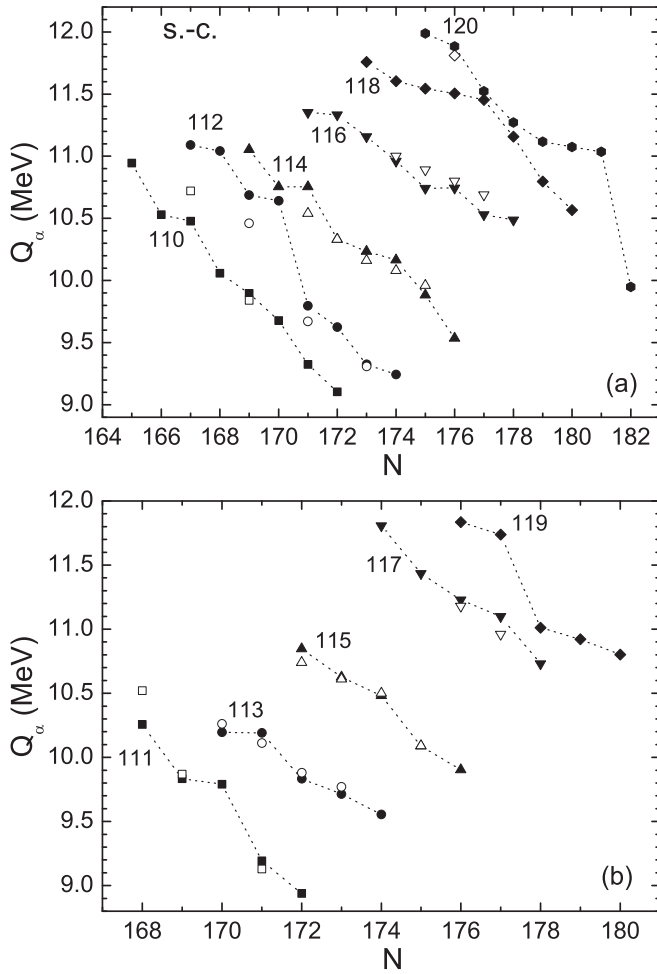


FIG. 2. Calculated  $\alpha$ -decay energies (closed symbols connected by lines) are compared with available experimental data (open symbols) [1,2,4,6] for (a) even- $Z$  and (b) odd- $Z$  nuclei with  $110 \leq Z \leq 120$ . The microscopic-macroscopic method is used with the Woods-Saxon potential extracted from the HFB self-consistent consideration.

treat only the isotopes of SHN, which can be reached in complete fusion reactions with available projectiles and targets. As seen in Fig. 2, the calculated  $Q_\alpha$  are in a good, within  $\approx 300$  keV, agreement with the available experimental  $Q_\alpha^{\text{exp}}$  [1,2,4,6]. The shell effects at  $Z = 114$  and  $N = 172$ – $176$  provide rather weak dependence of  $Q_\alpha$  on  $N$ . The strong role of the shell at  $N = 182$  is reflected in the well pronounced decrease of  $Q_\alpha$  at  $Z = 120$ . As in our calculations, the strong evidence of the shell closure at  $Z = 120$  and  $N = 182$ – $184$  was observed within the microscopic-macroscopic approach of Ref. [25]. For comparison, the  $Q_\alpha$  values predicted with microscopic-macroscopic model (FRDM2012) [23] are shown in Fig. 3. In contrast to our case, the  $Q_\alpha$ -value dependence on  $N$  is almost flat for the nuclei with  $Z = 116$ – $120$ . The weak shell effects at  $Z = 120$  and  $N = 182$  are also seen.

Note that in our consideration the nuclei  $^{295}119$  and  $^{295,297}120$  are expected to have  $Q_\alpha$  values of about 11.9 and 12.0, 11.5 MeV, respectively. These  $Q_\alpha$  values are close

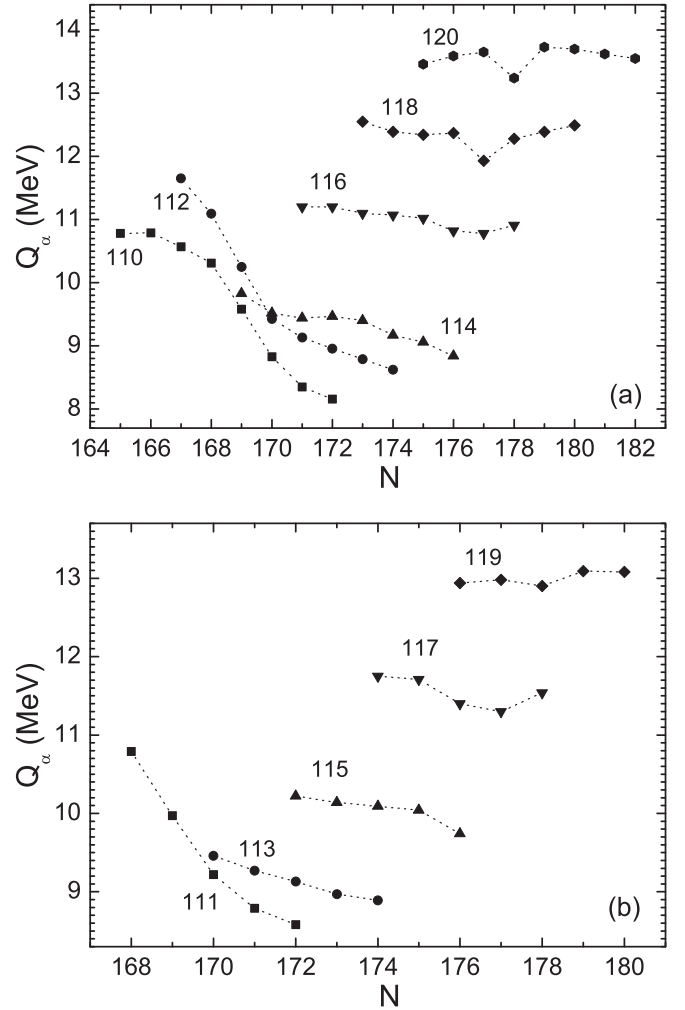


FIG. 3. The values of  $\alpha$ -decay energies (symbols connected by lines) calculated with the microscopic-macroscopic model (FRDM2012) [23] for (a) even- $Z$  and (b) odd- $Z$  nuclei with  $110 \leq Z \leq 120$ .

to those obtained with the microscopic-macroscopic method using the modified two-center shell model (TCSM) potential in the case when the parameters of the TCSM are adjusted for describing the known low-lying quasiparticle states of heaviest nuclei [24,25]. For the nuclei  $^{295}119$  and  $^{295,297}120$ , our  $Q_\alpha$  values are also close to those of the mass tables [74,75]. The microscopic-macroscopic model (FRDM2012) [23] results in  $Q_\alpha = 12.9$  MeV for  $^{295}119$  and  $Q_\alpha = 13.5, 13.7$  MeV for  $^{295,297}120$ . So, there is a strong difference (about 1–2 MeV) between the  $Q_\alpha$  values of the models with the FRDM2012 and self-consistent mean-field potentials.

## 2. Shell effects

For the nuclei produced in the  $\alpha$ -decay chains of  $^{295}119$  and  $^{295,297}120$ , the ground-state shell corrections calculated with the mean-field potential extracted here from the HFB approach [40] with the D3Y interaction are presented in Figs. 4 and 5. As found, the absolute values of the Strutinsky shell corrections become larger towards  $Z = 120$ . This is in

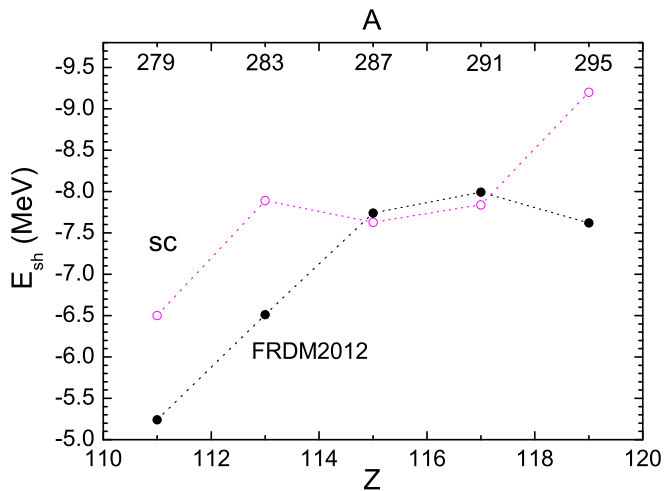


FIG. 4. The calculated ground-state shell corrections in the nuclei of  $\alpha$ -decay chain of  $^{295}\text{119}$ . The results are obtained with the microscopic-macroscopic method using the Woods-Saxon potential extracted from the self-consistent [sc] consideration (open circles). The microscopic corrections from the FRDM2012 [23] are shown by closed circles for comparison. The lines are drawn to guide an eye.

accordance with the results of self-consistent calculations in which the shell effects are stronger at  $Z = 120$  rather than at  $Z = 114$ . The shell corrections are pretty close to those obtained in the direct HFB calculations [40]. The ground-state shell corrections resulted from the HFB self-consistent approach are also close to those obtained with the microscopic-macroscopic method using the modified TCSM potential [24,25]. The calculations obtained with the TCSM provide us also stronger shell effects at  $Z = 120$  than at  $Z = 114$ .

For comparison, in Figs. 4 and 5 we present the microscopic corrections obtained with the FRDM2012 [23]. The parameters of the FRDM2012 are adjusted for the best global description of binding energies of known nuclei. For the  $Z = 120$  nucleus, the value of  $|E_{\text{sh}}|$  remains to be smaller in the FRDM2012 than that resulted from the HFB self-consistent approach (Fig. 5). The nuclei with  $Z = 116$  and  $118$  have the maximum absolute values of the shell corrections in the FRDM2012 model.

For the nuclei with  $Z = 119$  and  $120$ , the existing predictions of  $E_{\text{sh}}$  are varying and the experimental data are required to select the best suited microscopic approach. We noted that the predicted ground-state deformations are very close (within 10%) in all approaches used. Different parameter sets used as input for the HFB calculations result typically in different structures of heavy nuclei. So, the level order depends in some cases critically on the EDF underlying self-consistent approach. However, the shell closure at  $Z = 120$  is strongly supported in almost all self-consistent approaches while the neutron shell at  $N = 184$  depends on the model. We consider the nuclei for which the self-consistent approaches indicate stronger shell effects at  $Z = 120$  than at  $Z = 114$ , opposite to the known microscopic-macroscopic approaches [18,19,23]. Here, we show the possibility to obtain similar results with

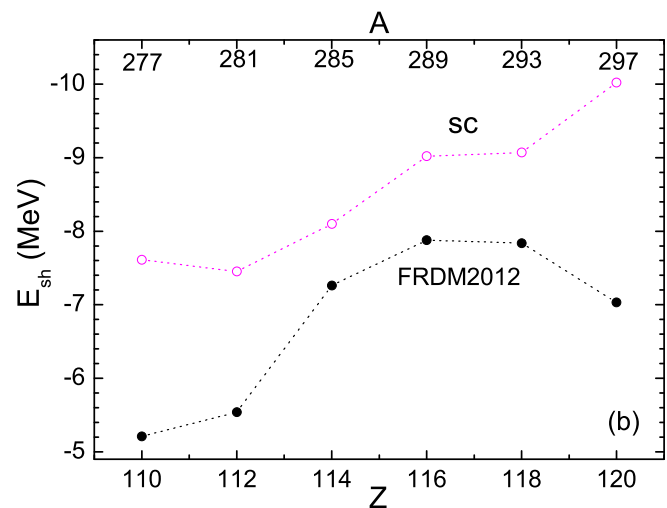
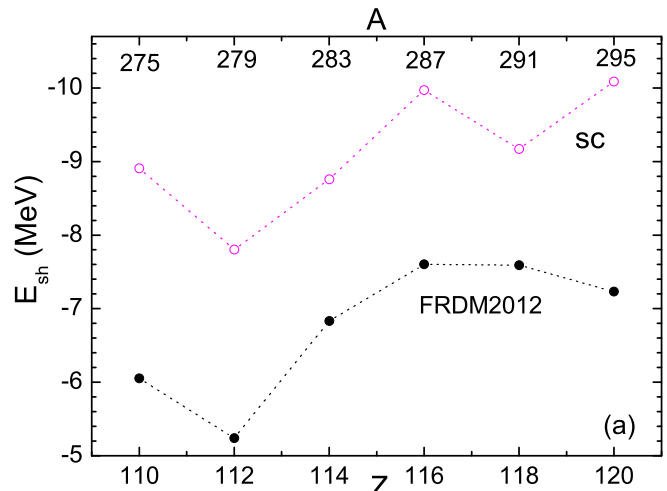


FIG. 5. The same as in Fig. 4, but for the nuclei of  $\alpha$ -decay chains of  $^{295,297}\text{120}$ .

the microscopic-macroscopic model and relate it to the self-consistent models.

### 3. Identification of elements $^{295}\text{119}$ and $^{295,297}\text{120}$ : Quasiparticle levels in nuclei of $\alpha$ -decay chains

One-quasiparticle excitations are calculated with the superfluid nuclear model using the variation principle and single-particle states in the deformed WS with equilibrium deformations  $\beta_{20}$  and  $\beta_{40}$  [26]. For neutron and proton, 100 and 70 single-particle states are used, respectively. The blocking effect is taken into consideration [26]. The quasiparticle energies are strongly affected not only by the mean-field single-particle levels, by the residual pairing and quasiparticle-phonon interactions. These interactions are taken into consideration with the quasiparticle-phonon model (QPM) [26] where we use the WS potential extracted from the HFB calculations. The ground-state deformations are included too. The quadrupole and octupole phonons and blocking effects in odd-even and even-odd nuclei are taken into account. In the region of heaviest nuclei, the density of the

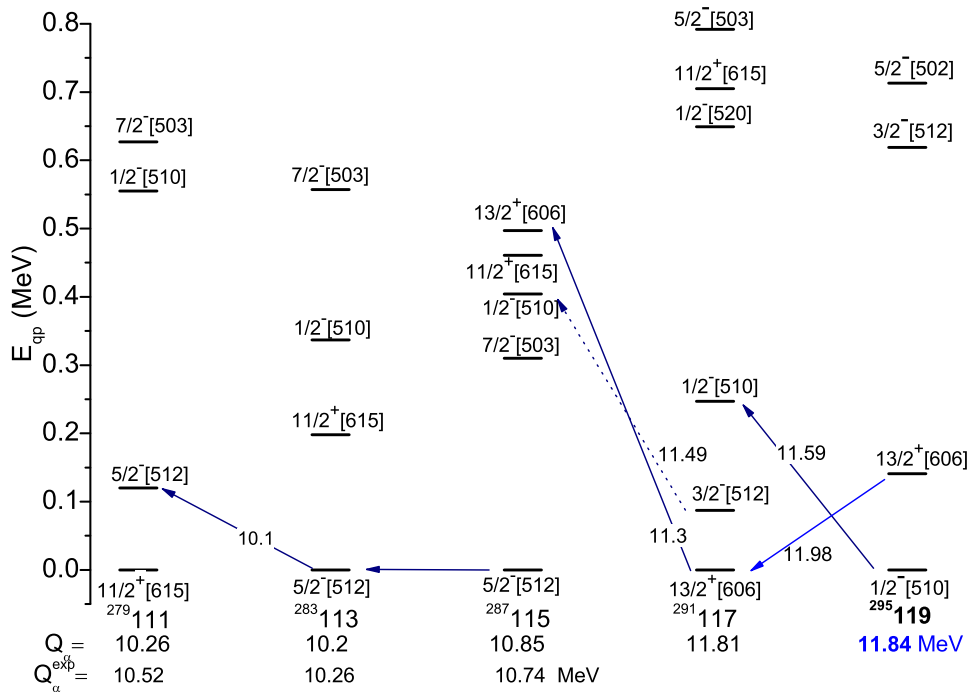


FIG. 6. Calculated energies of low-lying one-quasiproton states in the indicated nuclei of the  $\alpha$ -decay chain of  $^{295}\text{119}$ . The calculated values of  $Q_\alpha$  are for the ground-state-to-ground-state  $\alpha$ -decay. The  $\alpha$  decays with  $\Delta K = 0$  and  $\Delta K \neq 0$  are traced by solid and dashed arrows, respectively. The experimental values of  $Q_\alpha^{\text{exp}}$  are from Ref. [1].

single-particle states near the Fermi level is rather high and the quasiparticle-phonon interaction tend to increase the admixtures of one-quasiparticle components because the QPM core polarization effects induce couplings to three-quasiparticle configurations, described as quasiparticle-phonon states. The QPM provides a quite realistic description of the spectral structure of correlated one-quasiparticle states, which is important for the analysis of the  $\gamma$  transitions between these states. As a rule, the polarized low-lying quasiparticle states are typically dominated by a single component close to the unperturbed BCS eigenstate. However, the three-particle admixtures affect the  $\gamma$  transitions because they can occur through the admixture of components if the transition through the main component is hindered.

The one-quasiparticle spectra of odd-even nuclei with  $Z = 119$  and  $120$ , which are produced in the reactions studied below, are of special interest. In Fig. 6, the calculated one-quasiproton spectra and  $\alpha$  decays from the ground and possible isomeric states are shown in the nuclei of the  $\alpha$ -decay chain of the  $^{295}\text{119}$  nucleus. Because the WS potential resulted from the HFB calculation is deeper than those in the phenomenological microscopic-macroscopic models [19], it results in a sparser one-quasiparticle spectrum. Moreover, the shell effects increase considerably at  $Z = 120$ . The  $\alpha$ -decay chain of  $^{295}\text{119}$  contains the elements with  $Z \leq 115$  whose  $\alpha$ -decay energies are known experimentally [1]. The calculated and measured energies of  $\alpha$  decays of  $^{287}\text{Mc}$ ,  $^{283}\text{Nh}$ , and  $^{279}\text{Rg}$  are in a good agreement.

Because the parameters of single-particle potentials and spin-orbit interactions are different in Refs. [19,70], the order of one-quasiparticle levels is different as well. A remarkable

feature is that the existence of low-lying isomeric state is predicted by all single-particle potentials considered. As seen in Fig. 6, in the evaporation residue  $^{295}\text{119}$  the low-lying isomeric state  $13/2^+[606]$  can be populated with a probability close to the population probability of the ground state  $1/2^- [510]$ . In  $^{291}\text{Ts}$ , the state  $1/2^- [510]$  lies at 0.247 MeV, but the state  $13/2^+[606]$  is the ground state. Therefore, the possible  $\alpha$  decay of  $^{295}\text{119}$  from the isomeric  $13/2^+[606]$  and ground states easily occur into the corresponding states of  $^{291}\text{Ts}$ . So, two possible  $\alpha$  decays of  $^{295}\text{119}$  are expected to have different energies and half-lives. The difference of  $Q_\alpha$  by 0.4 MeV results in about one order of magnitude different half-lives. In comparison with the results of Ref. [70], the  $\alpha$  decay of the ground state of  $^{295}\text{119}$  occurs faster.

In  $^{291}\text{Ts}$ , both the ground  $13/2^+[606]$  and isomeric  $3/2^- [512]$  states are populated in the  $\alpha$ -decay chain of  $^{295}\text{119}$ . The  $\alpha$  decays from these states are hindered because of the structure of  $^{287}\text{Mc}$  calculated where the  $13/2^+[606]$  state is about 0.5 MeV and  $3/2^- [512]$  state has  $E_{pq} > 1$  MeV. So, the future data on the  $\alpha$  decay of  $^{291}\text{Ts}$  would be useful to conclude if the predictions of Ref. [70], where an unhindered  $\alpha$  decay is expected, or the present predictions are reliable. The  $\alpha$  decays of  $^{287}\text{Mc}$ ,  $^{283}\text{Nh}$ , and  $^{279}\text{Rg}$  are unhindered. The shell corrections in  $^{295}\text{119}$  and  $^{291}\text{Ts}$  are stronger than those for neighboring nuclei with  $Z = 120$  and  $118$  in Ref. [76] and their lifetimes with respect to fission are expected larger than 0.1 s. So, the  $\alpha$ -decay chain of  $^{295}\text{119}$  is likely to be interrupted by fission below  $^{279}\text{Rg}$ .

The possible  $\alpha$ -decay chain of the  $^{295}\text{120}$  nucleus is presented in Fig. 7. In  $^{295}\text{120}$ , the  $\alpha$  decay from the ground state  $1/2^+[611]$  is hindered by the relatively high energy

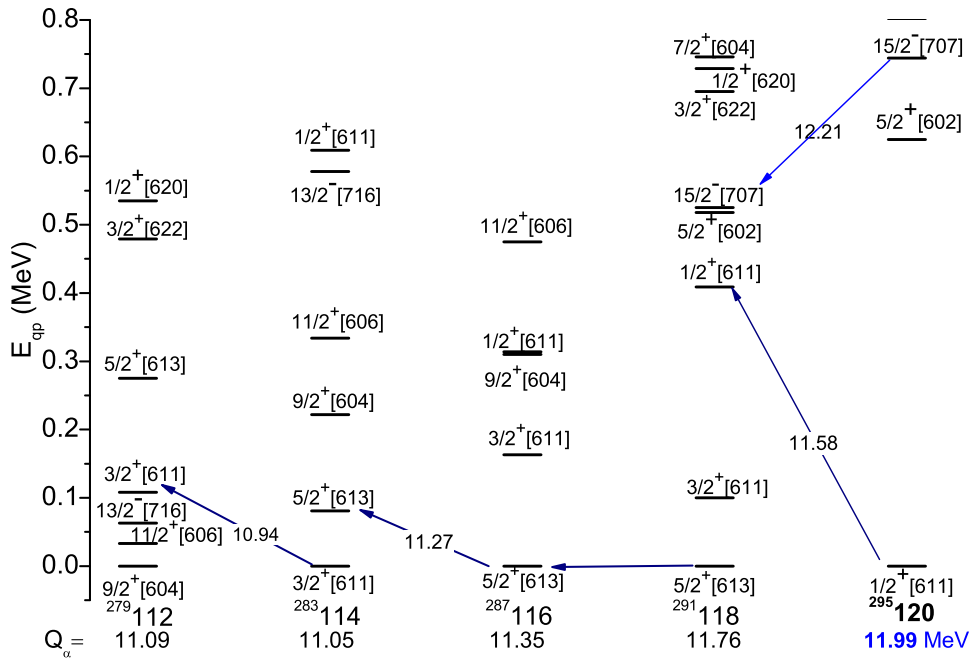


FIG. 7. The same as in Fig. 6, but for the nuclei of  $\alpha$ -decay chain of  $^{295}\text{120}$ .

of the  $1/2^+[611]$  state in  $^{291}\text{Og}$ . The  $\alpha$  decay from the isomeric  $15/2^- [707]$  state occurs if this state lives longer than 0.85 ms, which is quite improbable because it has energy about 0.75 MeV and can be coupled with many states. In accordance with Ref. [76], the  $^{295}\text{120}$  nucleus lives longer than 0.1 s with respect to spontaneous fission. So, the  $\alpha$  decay of  $^{295}\text{120}$  likely occurs in  $T_\alpha \approx 20$  ms with  $Q_\alpha = 11.58$  MeV. The  $\alpha$  decays of  $^{291}\text{Og}$ ,  $^{287}\text{Lv}$ , and  $^{283}\text{Fl}$  occur from the

ground states. Thus, the interruption of  $\alpha$ -decay chain in Fig. 7 occurs below  $^{279}\text{Cn}$ .

Comparing Figs. 7 and 8, we see that the shell effects are stronger when the neutron number approaches  $N = 172$ . In Fig. 8, there are no isomeric states in  $^{297}\text{120}$  and  $^{293}\text{Og}$ . So, the  $\alpha$  decay of  $^{297}\text{120}$  is expected only from the ground state. The  $\alpha$  decay of  $^{293}\text{Og}$  from the ground state is slightly hindered because the state  $5/2^+[602]$  in  $^{289}\text{Lv}$  has high

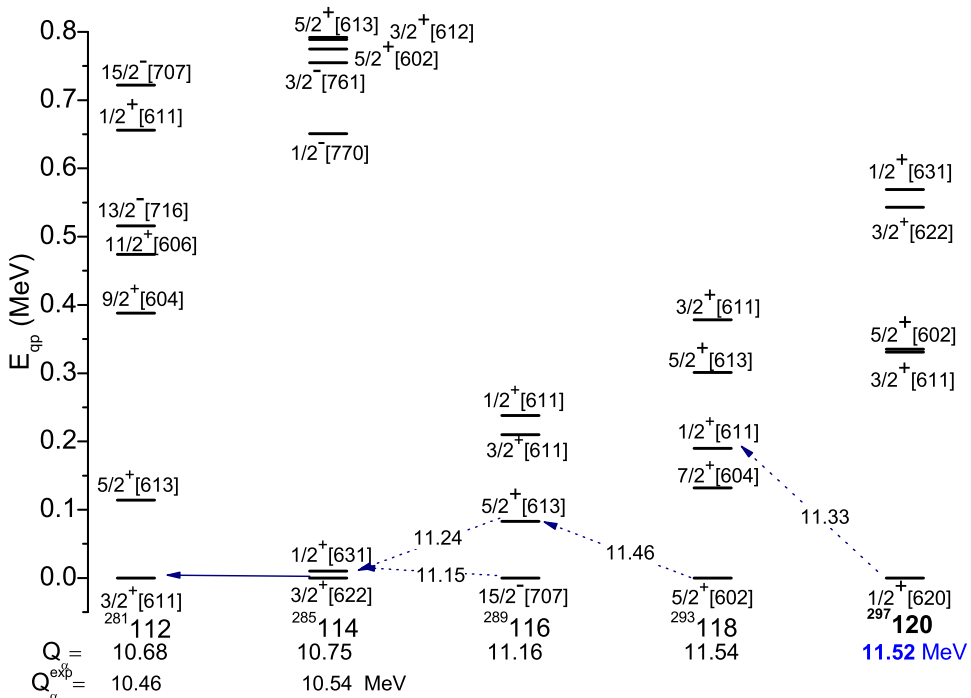


FIG. 8. The same as in Fig. 6, but for the nuclei of  $\alpha$ -decay chain of  $^{297}\text{120}$ .

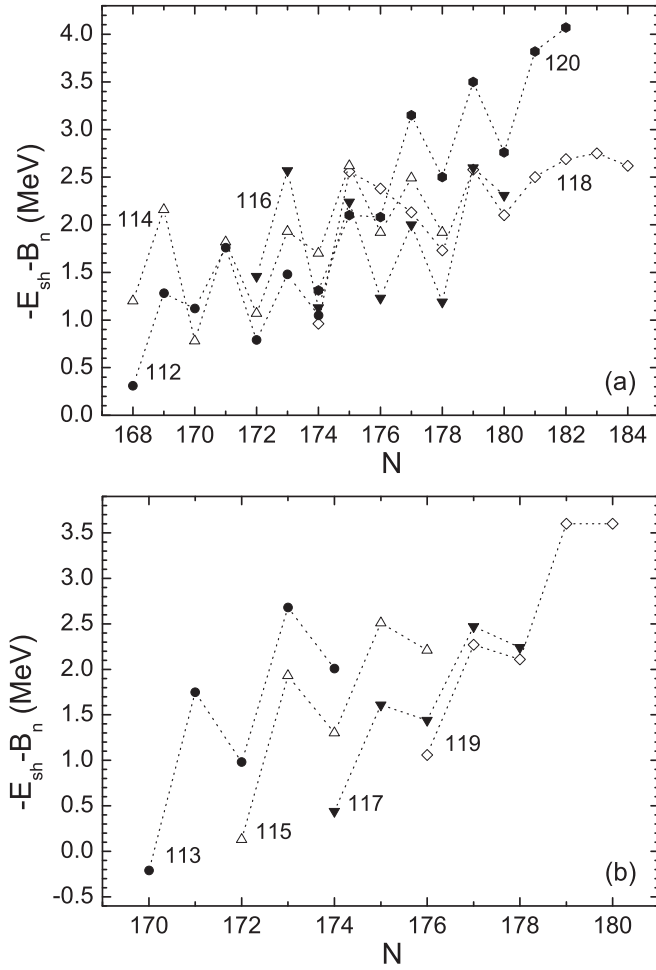


FIG. 9. The isotopic dependence of the value of  $B_f - B_n$ . The results are obtained with the microscopic-macroscopic method using the Woods-Saxon potential extracted from the self-consistent consideration. The fission barrier  $B_f$  is assumed to be an absolute value of the shell correction in the ground state of the nucleus. The results for the isotopes related to the indicated (a) even- $Z$  and (b) odd- $Z$  are shown by symbols connected by lines.

energy and the  $\alpha$  decay likely occurs to the state  $5/2^+$  [613]. So, in the  $\alpha$ -decay chain of the  $^{297}120$  the isomeric state  $5/2^+$  [613] in  $^{289}\text{Lv}$  is populated. From this state the  $\alpha$  decay with  $\Delta K = 2$  likely occur into the  $1/2^+$  [631] state of  $^{285}\text{Fl}$ . The  $\alpha$  decay of the ground state of  $^{289}\text{Lv}$  is strongly hindered because there is no low-lying  $15/2^-$  [707] state in  $^{285}\text{Fl}$  and  $\Delta K = 6-7$  for the decay to the low-lying states. Rough estimates of the values of  $T_\alpha$  for nuclei listed in Fig. 8 result in the value larger than 50 ms while the expected time for spontaneous fission is much longer. So, the interruption of  $\alpha$ -decay chain in Fig. 8 occurs below  $^{285}\text{Fl}$ .

### B. Fusion-evaporation reactions for the production of SHN

The DNS fusion model [53–70] describes successfully fusion-evaporation reactions especially related to the production of SHN. In the DNS model, the fusion is considered as a diffusion in the mass asymmetry coordinate  $\eta = (A_1 -$

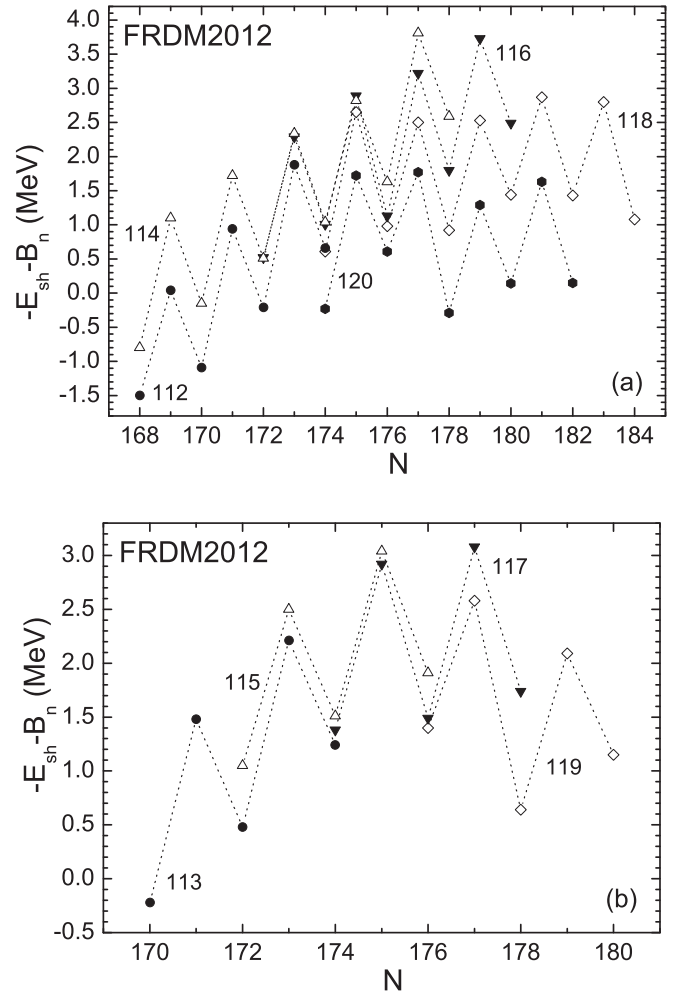


FIG. 10. The same as in Fig. 9, but for the nuclei from the FRDM2012 mass table [23].

$A_2)/(A_1 + A_2)$  ( $A_1$  and  $A_2$  are the mass numbers of the DNS nuclei). The evaporation residue cross section in  $xn$  evaporation channel is determined as

$$\sigma_{\text{ER}}^{xn}(E_{\text{c.m.}}) = \sum_J \sigma_c(E_{\text{c.m.}}, J) P_{\text{CN}}(E_{\text{c.m.}}, J) W_{\text{sur}}^{xn}(E_{\text{c.m.}}, J). \quad (19)$$

The capture cross section  $\sigma_c(E_{\text{c.m.}}, J)$  defines the transition of the colliding nuclei through the Coulomb barrier and the formation of the DNS when the kinetic energy above the barrier is transformed into the excitation energy of the DNS and the angular momentum  $J$  of the relative motion is redistributed in the DNS. For the reactions considered here, the maximum evaporation residue cross sections occur at energies  $E_{\text{c.m.}}$  at which all orientations of deformed nuclei contribute to the fusion. Therefore, in our case there is no noticeable loss of the cross section during the capture.

The probability of complete fusion  $P_{\text{CN}}(E_{\text{c.m.}}, J)$  depends on the competition between the complete fusion and quasi-fission after the capture stage. This competition can strongly reduce the value of  $\sigma_{\text{ER}}^{xn}(E_{\text{c.m.}})$ . The survival probability  $W_{\text{sur}}^{xn}$  takes into consideration the cooling down of the compound



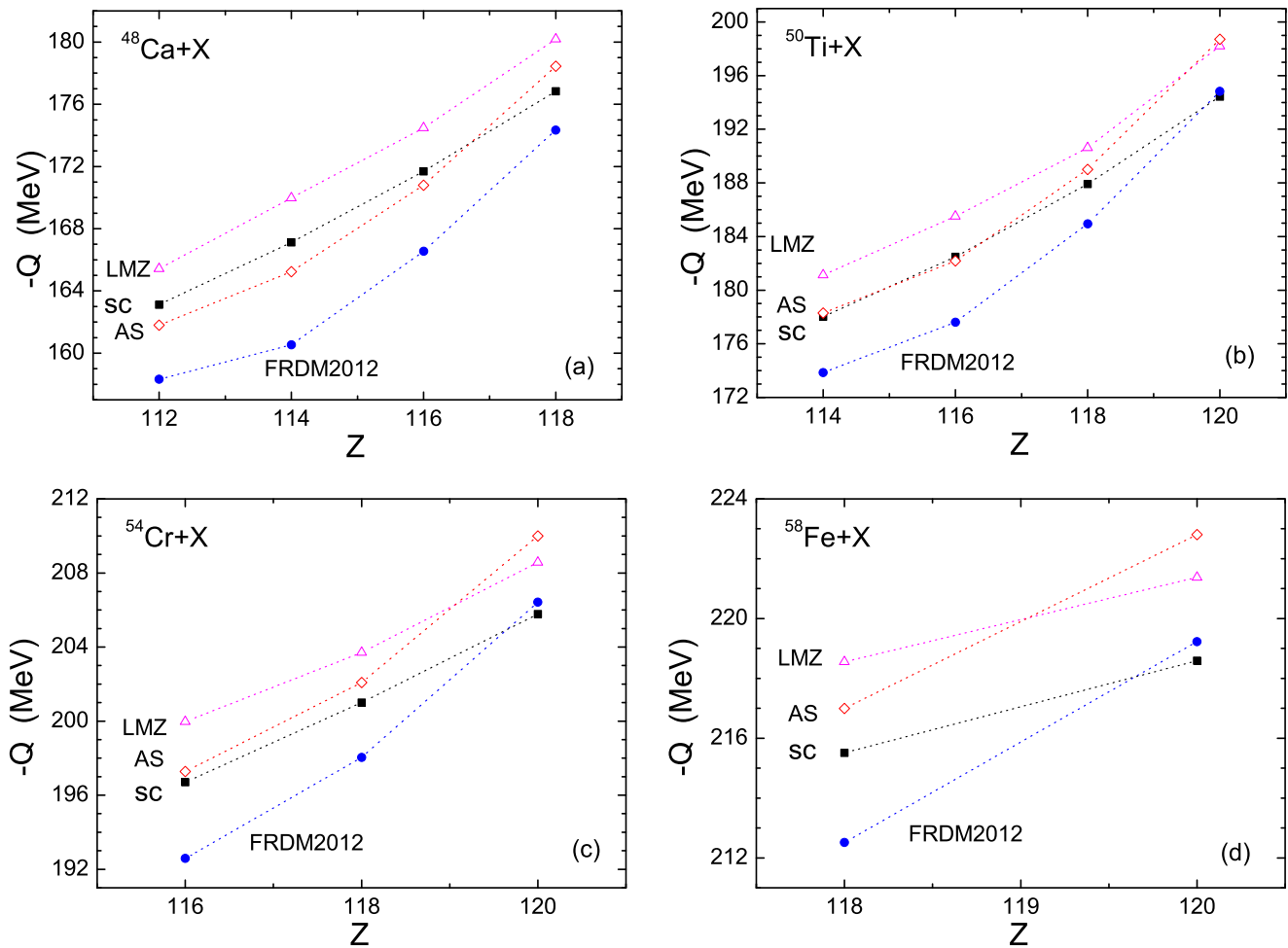


FIG. 11. The  $Q$  values for complete fusion calculated in the indicated reactions  $^{48}\text{Ca}$ ,  $^{50}\text{Ti} + ^{238}\text{U}$ ,  $^{244}\text{Pu}$ ,  $^{248}\text{Cm}$ ,  $^{249}\text{Cf}$ ,  $^{54}\text{Cr} + ^{238}\text{U}$ ,  $^{244}\text{Pu}$ ,  $^{248}\text{Cm}$ , and  $^{58}\text{Fe} + ^{238}\text{U}$ ,  $^{244}\text{Pu}$ , with the mass excesses of compound nuclei  $Z$  from the microscopic-macroscopic method with the Woods-Saxon potential extracted from the self-consistent consideration (sc, solid squares), Ref. [23] (FRDM2012, solid circles), Ref. [19] (AS, open diamonds), and Ref. [74] (LMZ, open triangles).

nucleus by emission of  $x$  neutrons in the competition with fission. The detailed description of the calculations of  $\sigma_c$ ,  $P_{\text{CN}}$ , and  $W_{\text{sur}}^{xn}$  is given in Ref. [69]. As estimated, the uncertainty of our calculated cross sections is within a factor of 2–4.

### 1. $B_f - B_n$ in SHN

The survival probability of compound nucleus strongly depends on the difference  $B_f - B_n$ , where  $B_f$  and  $B_n$  are the height of fission barrier and the neutron separation energy, respectively. As we know from previous works, the value of  $B_f$  correlates with  $-E_{\text{sh}}$  in heaviest nuclei. The value of  $B_f$  is mainly determined by the amplitude of the shell correction  $E_{\text{sh}}$  in the ground state of nuclei considered. So, we assume  $B_f = -E_{\text{sh}}$  to be consistent with our previous calculations. In many cases of interest,  $|E_{\text{sh}}| - B_f$  is less than 0.7 MeV in the FRDM(2012) [23]. Because of the damping of the shell corrections, this difference has minor influence on the final results. Moreover, the level density parameter is set to describe the cross section for production of FI in

the  $4n$ -evaporation channel. This setting takes effectively into account the deviation from the assumption  $B_f = -E_{\text{sh}}$ .

As a result, the shell effects prevent the fission of superheavy nuclei and the value of  $B_f \approx -E_{\text{sh}}$  strongly depends on the neutron and proton numbers of the compound nucleus, especially, on how close they are to the magic numbers. At fixed charge number the predicted values of  $B_n$  steadily decrease in the region of  $N \geq 170$  with increasing  $N$ . The values of  $B_n$  predicted with different models vary within 0.5 MeV and the shell effects cause the difference in the  $B_f - B_n$  calculated with our and the FRDM2012 models (Figs. 9 and 10).

As seen in Fig. 10, the microscopic-macroscopic model [23] provides the closed proton shell at  $Z = 114$  and the fission barrier grows with  $N$  up to  $N = 178$ – $180$ . At fixed neutron number and  $Z > 114$ , the height of the fission barrier decreases with increasing  $Z$ . In Fig. 9, the fission barrier increases when  $N$  approaches  $N = 184$ . The nuclei with  $Z = 120$  and  $N = 180$ – $182$ , where the fission barriers are rather high, are expected to be the most stable nuclei beyond those with  $Z = 114$  and  $N = 176$ – $178$ . Note that the shell closure at

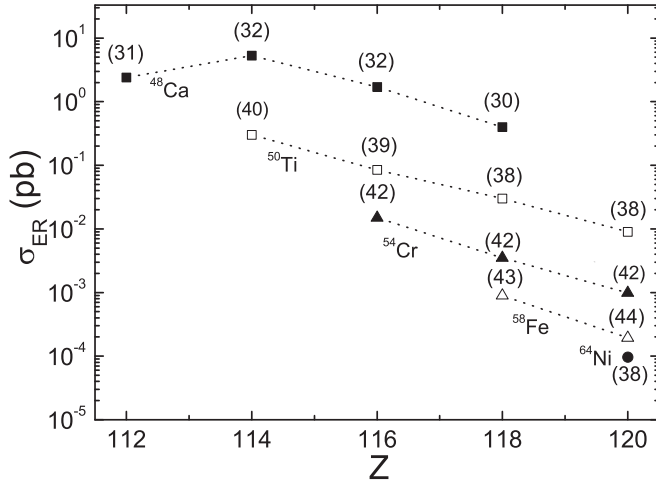


FIG. 12. The evaporation residue cross sections in the maxima of excitation functions versus charge number  $Z$  for the reactions  $^{48}\text{Ca}$ ,  $^{50}\text{Ti} + ^{238}\text{U}$ ,  $^{244}\text{Pu}$ ,  $^{248}\text{Cm}$ ,  $^{249}\text{Cf}$ ,  $^{54}\text{Cr} + ^{238}\text{U}$ ,  $^{244}\text{Pu}$ ,  $^{248}\text{Cm}$ ,  $^{58}\text{Fe} + ^{238}\text{U}$ ,  $^{244}\text{Pu}$ , and  $^{64}\text{Ni} + ^{238}\text{U}$ . The predicted properties of SHN are used from the microscopic-macroscopic method with the Woods-Saxon potential extracted from the self-consistent consideration. The excitation energies in MeV of compound nuclei are given in brackets.

$Z = 120$  results also from the relativistic mean-field models [34,35].

## 2. Fusion $Q$ values

For the complete fusion reactions  $^{48}\text{Ca}$ ,  $^{50}\text{Ti} + ^{238}\text{U}$ ,  $^{244}\text{Pu}$ ,  $^{248}\text{Cm}$ ,  $^{249}\text{Cf}$ ,  $^{54}\text{Cr} + ^{238}\text{U}$ ,  $^{244}\text{Pu}$ ,  $^{248}\text{Cm}$ , and  $^{58}\text{Fe} + ^{238}\text{U}$ ,  $^{244}\text{Pu}$ , we calculate the  $Q$  values (Fig. 11) with different predictions of binding energies of compound nucleus. One can see that our results are within the existing uncertainty of 5–7 MeV provided by previous calculations. For smaller  $Z$ , they are close to the results obtained with the data of Ref. [74]. For larger  $Z$ , our calculated  $Q$  values approach those obtained with the microscopic-macroscopic model [23]. So, the uncertainty of the  $Q$  value leads to an uncertainty in excitation energy of compound nuclei in the range of 5–7 MeV, which, in fact, is close to the neutron separation energy.

## 3. Predictions of evaporation residue cross sections

Using our predictions of  $M_{lh}$ ,  $E_{sh}$ , and  $B_n$ , we calculated the evaporation residue cross sections in the reactions  $^{48}\text{Ca}$ ,  $^{50}\text{Ti} + ^{238}\text{U}$ ,  $^{244}\text{Pu}$ ,  $^{248}\text{Cm}$ ,  $^{249}\text{Cf}$ ,  $^{54}\text{Cr} + ^{238}\text{U}$ ,  $^{244}\text{Pu}$ ,  $^{248}\text{Cm}$ ,  $^{58}\text{Fe} + ^{238}\text{U}$ ,  $^{244}\text{Pu}$ , and  $^{64}\text{Ni} + ^{238}\text{U}$  (Fig. 12). In the reactions  $^{48}\text{Ca} + ^{238}\text{U}$ ,  $^{248}\text{Cm}$ ,  $^{249}\text{Cf}$  the experimental values of  $\sigma_{ER}^{3n}$  are 0.5–2.5 pb, about 1 pb, and 0.5 pb [1], respectively. Thus, the difference between the calculated and experimental  $\sigma_{ER}$  are within the experimental and theoretical uncertainties. A good description of the existing data indicates reliability of the predictions for the reactions with projectiles heavier than  $^{48}\text{Ca}$ . In comparison to our previous calculations [68] with the mass table of Ref. [18], the values of  $\sigma_{ER}$  decreases slower with increasing

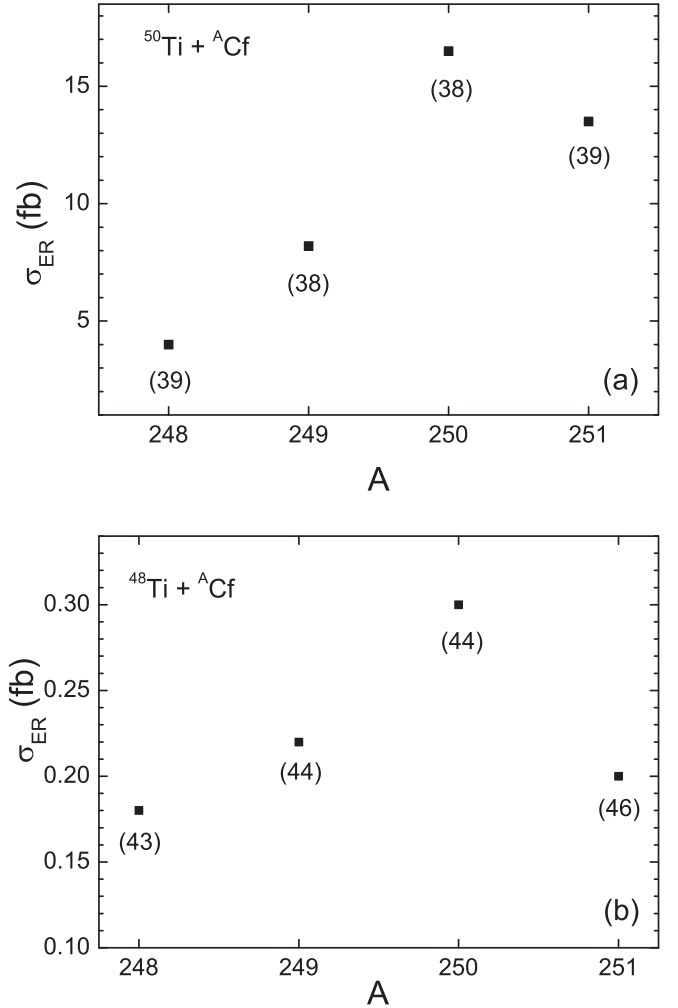


FIG. 13. The same as in Fig. 12, but for the reactions (a)  $^{50}\text{Ti} + ^A\text{Cf}$  and (b)  $^{48}\text{Ti} + ^A\text{Cf}$ .

$Z$ . The stronger shell effect revealed here for nuclei with  $Z > 118$  result in larger survival probabilities and larger values of  $\sigma_{ER}$ .

With  $^{50}\text{Ti}$  beam the values of  $\sigma_{ER}$  for the nuclei with  $Z = 114$ – $118$  are expected to be  $\approx 10$  times smaller than those with  $^{48}\text{Ca}$  beam (Fig. 12). The main reason for this is the decrease of  $P_{CN}$  in Eq. (19) with mass asymmetry in the entrance channel of reaction. With  $^{50}\text{Ti}$  the nucleus  $^{295}120$  is predicted to be produced with the maximum cross section of  $\approx 8$  fb. For the production of nucleus with  $Z = 120$ , the beams  $^{54}\text{Cr}$ ,  $^{58}\text{Fe}$ , and  $^{64}\text{Ni}$  would lead to smaller cross sections. For example, in the  $^{54}\text{Cr} + ^{248}\text{Cm}$  reaction,  $\sigma_{ER} \approx 1$  fb.

We calculated the evaporation residue cross sections in the reactions  $^{50}\text{Ti} + ^A\text{Cf}$  ( $A = 248$ – $251$ ) leading to the compound nuclei with  $Z = 120$  (Fig. 13). As in Refs. [64–66], the value of  $\sigma_{ER}$  changes within factor 2–4 in the treated interval of mass numbers  $A$ . The values of  $\sigma_{ER}$  are almost the same (about 15 fb) in the cases of  $^{250}\text{Cf}$  and  $^{251}\text{Cf}$  targets. In the case of  $^{249}\text{Cf}$  target and  $^{50}\text{Ti}$  beam, the value of  $\sigma_{ER}$  is smaller than those in the reactions  $^{50}\text{Ti} + ^{250,251}\text{Cf}$ , about 8 fb. For the production of nuclei with  $Z = 120$ , the reactions with  $^{50}\text{Ti}$

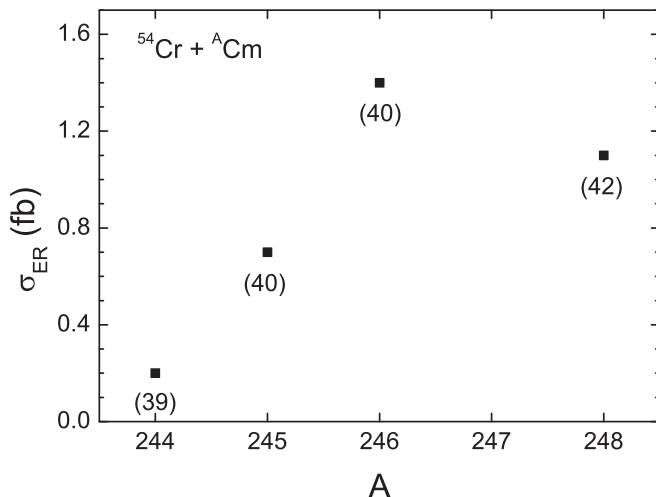


FIG. 14. The same as in Fig. 12, but for the reactions  $^{54}\text{Cr} + {}^A\text{Cm}$ .

are favorable over those with  $^{48}\text{Ti}$ . The optimal excitation energies in the reactions with  $^{50}\text{Ti}$  are about 4–7 MeV smaller than in those with  $^{48}\text{Ti}$ . As a result, the survival probabilities and, correspondingly, the production cross sections are larger in the  $^{50}\text{Ti}$  reactions. Note that for the same reason the difference is relatively small between the cross sections in the reactions  $^{58}\text{Fe} + {}^{244}\text{Pu}$  and  $^{64}\text{Ni} + {}^{238}\text{U}$  (Fig. 12).

In the reactions  $^{54}\text{Cr} + {}^A\text{Cm} \rightarrow 120$ , the value of  $\sigma_{ER}$  decreases by factor of about 2 with the mass number of target-nucleus from  $A = 248$  to  $A = 245$  (Fig. 14). In the reactions  $^{50}\text{Ti} + {}^{249}\text{Bk}$ , the nucleus 119 is predicted to be produced with the maximum cross section 19 fb (Fig. 15). The increase of  $\sigma_{ER}$  with  $A$  is mostly due to the increase of the survival probability. In the  $4n$  evaporation channels of the reactions  $^{50}\text{Ti} + {}^{235,236,238}\text{U}$ , the predicted maximum production cross sections are about 0.2–0.5 pb (Fig. 16). These reactions can be measured and compared with the  $^{48}\text{Ca}$ -induced reactions.

Using different mass tables and assumptions, the existing fusion model predict the maximal evaporation residue

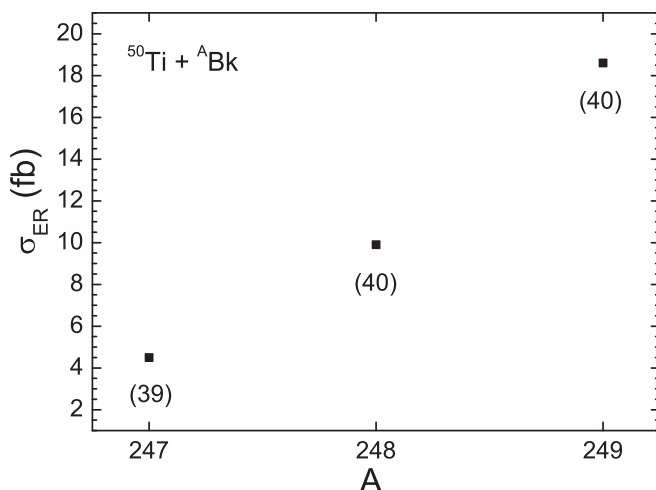


FIG. 15. The same as in Fig. 12, but for the reactions  $^{50}\text{Ti} + {}^A\text{Bk}$ .

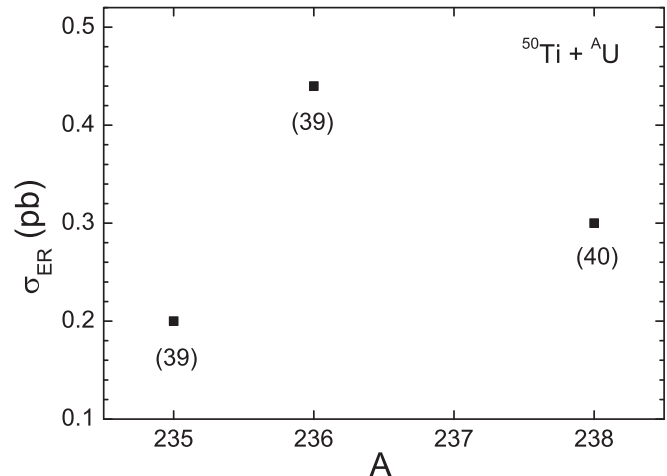


FIG. 16. The same as in Fig. 13, but for the reactions  $^{50}\text{Ti} + {}^A\text{U}$ .

cross sections of the order of 30–700 pb and 0.5–100 fb in the complete fusion reactions  $^{50}\text{Ti} + {}^{249}\text{Bk} \rightarrow 119$  and  $^{50}\text{Ti} + {}^{249}\text{Cf} \rightarrow 120$ , respectively [25,58,59,61,68,77–79]. For example, the evaporation residue cross sections calculated with the mass table [18] is about of 1 fb for 120 element [68]. In Ref. [25] ([78]), the predicted with mass table [25] ([21]) production cross sections of elements 119 and 120 are 40 fb (30 fb) and 23 fb (6 fb), respectively. More optimistic predictions (110 fb and 50 fb for 119 and 120 elements, respectively) are given in Ref. [61]. The large variation of cross sections in different models is mainly due to the different fusion and fission barriers, level density parameters, and  $Q$  values used in calculations.

## V. SUMMARY

The mean-field potentials extracted from the HFB calculations with the EDF of Ref. [40] were applied in the microscopic-macroscopic method [26] for calculating the ground-state shell corrections, the mass excesses, and  $Q_\alpha$  values in the superheavy nuclei with  $Z = 112$ –120. We found that the self-consistent approach provides deeper single-particle potentials that those used in the phenomenological consideration and endorses the stronger shell effects at  $Z = 120$  rather than those at  $Z = 114$ . The reason for these potential differences is mainly related to the inclusion of momentum dependent effects. In the self-consistent potentials the momentum dependence, i.e., nonlocality, of the underlying microscopic mean-field self-energies is accounted for by taking an average over the Fermi sphere. So, our microscopic-macroscopic treatment qualitatively leads to the results close to those in the self-consistent mean-field treatments. The spectra of low-lying nonrotational states in the nuclei of  $\alpha$ -decay chains of  $^{295}119$  and  $^{295,297}120$  were studied. Based on the calculated one-quasiproton spectra and energies for  $\alpha$  decays, we could explain why the  $\alpha$ -decay chain of  $^{295}119$  or  $^{291}\text{Ts}$ , or  $^{287}\text{Mc}$  is terminated by spontaneous fission of  $^{267}\text{Db}$ . In addition, the number of isomeric states in the heaviest odd- $Z$  nuclei were predicted. In the  $^{295}119$  nucleus, for example, we expect the low-lying isomeric state  $13/2^+[606]$ . The  $\alpha$ -decays

from some of the isomeric states seem to be possible, resulting in a possible spread of the  $\alpha$  energies across an energy window of almost 0.7 MeV. The  $\alpha$ -decay  $Q_\alpha$  values of nuclei belonging to the  $\alpha$ -decay chain of  $^{295}119$  and  $^{295,297}120$  were obtained and compared with the available experimental data. A rather good description of the data was demonstrated. The  $Z = 120$  nuclei with  $N = 175$ – $179$  are predicted to have  $Q_\alpha$  about 12.0–11.2 MeV and lifetimes about 3 ms–0.2 s. These  $Q_\alpha$  are in fair agreement with Refs. [74,75] and about 2 MeV smaller than in Refs. [19,23]. The experimental measurement of  $Q_\alpha$  for at least one isotope of  $Z = 120$  nucleus would help tremendously to countercheck the theoretical calculations and, if necessary, to adjust parameters to the proper shell structure of the SHN with  $Z > 118$ .

According to our predictions for the SHN, one can expect the production of evaporation residues with  $Z = 119$  and  $120$  in the reactions  $^{50}\text{Ti} + ^{249}\text{Bk}$  and  $^{50}\text{Ti} + ^{249}\text{Cf}$  with the cross sections 19 and 8 fb, respectively. Note that the definition of maxima of the excitation functions provides a good test for the predictions of the models as well.

#### ACKNOWLEDGMENTS

This work was supported in part by DFG, RFBR(17-52-12015), and RFBR(20-02-00176). The IN2P3 (France)-JINR (Dubna), and Polish - JINR (Dubna) Cooperation Programmes are gratefully acknowledged. The work of N.V.A. was supported by Tomsk Polytechnic University Competitiveness Enhancement Program grant.

- 
- [1] Yu. Ts. Oganessian, *J. Phys. G* **34**, R165 (2007).  
 [2] Yu. Ts. Oganessian and V. K. Utyonkov, *Nucl. Phys. A* **944**, 62 (2015).  
 [3] V. K. Utyonkov *et al.*, *Phys. Rev. C* **92**, 034609 (2015).  
 [4] S. Hofmann *et al.*, *Eur. Phys. J. A* **32**, 251 (2007).  
 [5] R. Eichler *et al.*, *Nature (London)* **447**, 72 (2007).  
 [6] L. Stavsetra, K. E. Gregorich, J. Dvorak, P. A. Ellison, I. Dragojevic, M. A. Garcia, and H. Nitsche, *Phys. Rev. Lett.* **103**, 132502 (2009).  
 [7] Ch. Düllmann *et al.*, *Phys. Rev. Lett.* **104**, 252701 (2010).  
 [8] J. M. Gates *et al.*, *Phys. Rev. C* **83**, 054618 (2011).  
 [9] S. Heinz *et al.*, *J. Phys. Conf. Ser.* **282**, 012007 (2011).  
 [10] S. Hofmann *et al.*, *Eur. Phys. J. A* **48**, 62 (2012).  
 [11] J. M. Khuyagbaatar *et al.*, *Phys. Rev. Lett.* **112**, 172501 (2014).  
 [12] Yu. Ts. Oganessian *et al.*, *Phys. Rev. C* **79**, 024603 (2009).  
 [13] S. Hofmann *et al.*, *Eur. Phys. J. A* **52**, 180 (2016); **52**, 116 (2016).  
 [14] R.-D. Herzberg and P. T. Greenlees, *Prog. Part. Nucl. Phys.* **61**, 674 (2008); R.-D. Herzberg and D. M. Cox, *Radiochim. Acta* **99**, 441 (2011).  
 [15] S. Hofmann and G. Münzenberg, *Rev. Mod. Phys.* **72**, 733 (2000).  
 [16] A. Sobczewski, F. A. Gareev, and B. N. Kalinkin, *Phys. Lett. B* **22**, 500 (1966); W. D. Myers and W. J. Swiatecki, *Nucl. Phys.* **81**, 1 (1966); H. Meldner, *Ark. Fys.* **36**, 593 (1967); S. G. Nilsson *et al.*, *Nucl. Phys. A* **115**, 545 (1968); U. Mosel and W. Greiner, *Z. Phys. A* **222**, 261 (1969); F. O. Fiset and R. J. Nix, *Nucl. Phys. A* **193**, 647 (1972); P. Möller, S. G. Nilsson, and R. J. Nix, *ibid.* **229**, 292 (1974); J. Randrup *et al.*, *Phys. Rev. C* **13**, 229 (1976); P. Möller and R. J. Nix, *J. Phys. G* **20**, 292 (1994); A. Sobczewski, *Phys. Part. Nuclei* **25**, 295 (1994); R. Smolanczuk, J. Skalski, and A. Sobczewski, *Phys. Rev. C* **52**, 1871 (1995).  
 [17] P. Möller and R. Nix, *At. Data Nucl. Data Tables* **39**, 213 (1988).  
 [18] P. Möller, J. R. Nix, W. D. Myers, and W. J. Swiatecki, *At. Data Nucl. Data Tables* **59**, 185 (1995).  
 [19] I. Muntian, Z. Patyk, and A. Sobczewski, *Acta. Phys. Pol. B* **32**, 691 (2001); **34**, 2141 (2003); **34**, 2073 (2003); I. Muntian, S. Hofmann, Z. Patyk, and A. Sobczewski, *Phys. Atom. Nucl.* **66**, 1015 (2003); A. Parkhomenko, I. Muntian, Z. Patyk, and A. Sobczewski, *Acta. Phys. Pol. B* **34**, 2153 (2003); A. Parkhomenko and A. Sobczewski, *ibid.* **36**, 3095 (2005); A. Sobczewski and K. Pomorski, *Prog. Part. Nucl. Phys.* **58**, 292 (2007); A. Sobczewski, *Phys. Rev. C* **94**, 051302(R) (2016).  
 [20] P. Jachimowicz, M. Kowal, and J. Skalski, *Phys. Rev. C* **89**, 024304 (2014).  
 [21] M. Kowal, P. Jachimowicz, and A. Sobczewski, *Phys. Rev. C* **82**, 014303 (2010); M. Kowal, P. Jachimowicz, and J. Skalski, *arXiv:1203.5013*; P. Jachimowicz, M. Kowal, and J. Skalski, *Phys. Rev. C* **95**, 014303 (2017).  
 [22] P. Möller, A. J. Sierk, T. Ichikawa, A. Iwamoto, R. Bengtsson, H. Uhrenholt, and S. Aberg, *Phys. Rev. C* **79**, 064304 (2009).  
 [23] P. Möller, A. J. Sierk, T. Ichikawa, and H. Sagawa, *At. Data Nucl. Data Tables* **109-110**, 1 (2016).  
 [24] G. G. Adamian, N. V. Antonenko, and W. Scheid, *Phys. Rev. C* **81**, 024320 (2010); G. G. Adamian, N. V. Antonenko, S. N. Kuklin, and W. Scheid, *ibid.* **82**, 054304 (2010).  
 [25] A. N. Kuzmina, G. G. Adamian, N. V. Antonenko, and W. Scheid, *Phys. Rev. C* **85**, 014319 (2012).  
 [26] G. G. Adamian, L. A. Malov, N. V. Antonenko, and R. V. Jolos, *Phys. Rev. C* **97**, 034308 (2018).  
 [27] W. Koepf and P. Ring, *Z. Phys. A* **339**, 81 (1991).  
 [28] K. Rutz, M. Bender, T. Burvenich, T. Schilling, P.-G. Reinhard, J. A. Maruhn, and W. Greiner, *Phys. Rev. C* **56**, 238 (1997); J. Decharge *et al.*, *Phys. Lett. B* **451**, 275 (1999).  
 [29] M. Bender, K. Rutz, P.-G. Reinhard, J. A. Maruhn, and W. Greiner, *Phys. Rev. C* **58**, 2126 (1998).  
 [30] M. Bender, K. Rutz, P.-G. Reinhard, J. A. Maruhn, and W. Greiner, *Phys. Rev. C* **60**, 034304 (1999).  
 [31] M. Bender, *Phys. Rev. C* **61**, 031302(R) (2000); M. Bender *et al.*, *Phys. Lett. B* **515**, 42 (2001); P. G. Reinhard, *Rep. Prog. Phys.* **52**, 439 (1989); P. Ring, *Prog. Part. Nucl. Phys.* **37**, 193 (1996); S. Cwiok *et al.*, *Nucl. Phys. A* **611**, 211 (1996); M. Bender, P. H. Heenen, and P. G. Reinhard, *Rev. Mod. Phys.* **75**, 121 (2003).  
 [32] A. Baran, *Phys. Rev. C* **61**, 024316 (2000).  
 [33] T. Burvenich, M. Bender, J. A. Maruhn, and P.-G. Reinhard, *Phys. Rev. C* **69**, 014307 (2004).  
 [34] J. Meng, J. Peng, S. Q. Zhang, and S.-G. Zhou, *Phys. Rev. C* **73**, 037303 (2006); J. Peng, H. Sagawa, S. Q. Zhang, J. M. Yao, Y. Zhang, and J. Meng, *ibid.* **77**, 024309 (2008).  
 [35] J. J. Li, W. H. Long, J. Margueron, and N. Van Giai, *Phys. Lett. B* **732**, 169 (2014).

- [36] A. T. Kruppa, M. Bender, W. Nazarewicz, P.-G. Reinhard, T. Vertse, and S. Cwiok, *Phys. Rev. C* **61**, 034313 (2000).
- [37] Y. Shi, D. E. Ward, B. G. Carlsson, J. Dobaczewski, W. Nazarewicz, I. Ragnarsson, and D. Rudolph, *Phys. Rev. C* **90**, 014308 (2014).
- [38] S.-G. Zhou, *Phys. Scr.* **91**, 063008 (2016).
- [39] Z.-X. Li, Z.-H. Zhang, and P.-W. Zhao, *Front. Phys.* **10**, 102101 (2015).
- [40] F. Hofmann and H. Lenske, *Phys. Rev. C* **57**, 2281 (1998).
- [41] H. Lenske and C. Fuchs, *Phys. Lett. B* **345**, 355 (1995).
- [42] S. A. Fayans, S. V. Tolokonnikov, E. L. Trykov, and D. Zawischa, *Nucl. Phys. A* **676**, 49 (2000).
- [43] S. V. Tolokonnikov, I. N. Borzov, M. Kortelainen, Yu. S. Lutostansky, and E. E. Saperstein, *Eur. Phys. J. A* **53**, 33 (2017).
- [44] A. Staszczak, A. Baran, J. Dobaczewski, and W. Nazarewicz, *Phys. Rev. C* **80**, 014309 (2009); J. A. Sheikh, N. Hinohara, J. Dobaczewski, T. Nakatsukasa, W. Nazarewicz, and K. Sato, *ibid.* **89**, 054317 (2014).
- [45] E. V. Litvinova and A. V. Afanasjev, *Phys. Rev. C* **84**, 014305 (2011).
- [46] H. Abusara, A. V. Afanasjev, and P. Ring, *Phys. Rev. C* **85**, 024314 (2012); S. E. Agbemava, A. V. Afanasjev, D. Ray, and P. Ring, *ibid.* **95**, 054324 (2017); Z. Shi, A. V. Afanasjev, Z. P. Li, and J. Meng, *ibid.* **99**, 064316 (2019).
- [47] J. Zhao, B.-N. Lu, T. Niksic, D. Vretenar, and S.-G. Zhou, *Phys. Rev. C* **93**, 044315 (2016); J. Zhao, T. Niksic, D. Vretenar, and S.-G. Zhou, *ibid.* **99**, 014618 (2019); J. Zhao, J. Xiang, Z.-P. Li, T. Niksic, D. Vretenar, and S.-G. Zhou, *ibid.* **99**, 054613 (2019).
- [48] M. Baldo, L. M. Robledo, P. Schuck, and X. Vinas, *Phys. Rev. C* **87**, 064305 (2013).
- [49] S. A. Giuliani, G. Martinez-Pinedo, and L. M. Robledo, *Phys. Rev. C* **97**, 034323 (2018).
- [50] M. Warda, A. Zdeb, and L. M. Robledo, *Phys. Rev. C* **98**, 041602(R) (2018).
- [51] P. Sarriguren, *Phys. Rev. C* **100**, 014309 (2019).
- [52] G. G. Adamian, L. A. Malov, N. V. Antonenko, H. Lenske, K. Wang, and S.-G. Zhou, *Eur. Phys. J. A* **54**, 170 (2018).
- [53] V. V. Volkov, *Izv. Akad. Nauk SSSR, Ser. Fiz.* **50**, 1879 (1986); N. V. Antonenko, E. A. Cherepanov, A. K. Nasirov, V. B. Permjakov, and V. V. Volkov, *Phys. Lett. B* **319**, 425 (1993); *Phys. Rev. C* **51**, 2635 (1995).
- [54] G. G. Adamian, N. V. Antonenko, S. P. Ivanova, and W. Scheid, *Nucl. Phys. A* **646**, 29 (1999).
- [55] G. G. Adamian, N. V. Antonenko, W. Scheid, and V. V. Volkov, *Nucl. Phys. A* **633**, 409 (1998); *Nuovo Cimento A* **110**, 1143 (1997).
- [56] G. G. Adamian, N. V. Antonenko, and W. Scheid, *Nucl. Phys. A* **678**, 24 (2000).
- [57] G. G. Giardina, S. Hofmann, A. I. Muminov, and A. K. Nasirov, *Eur. Phys. J. A* **8**, 205 (2000); G. G. Giardina, F. Hanappe, A. I. Muminov, A. K. Nasirov, and L. Stuttgé, *Nucl. Phys. A* **671**, 165 (2000); A. K. Nasirov *et al.*, *ibid.* **759**, 342 (2005); H. Q. Zhang, C. L. Zhang, C. J. Lin, Z. H. Liu, F. Yang, A. K. Nasirov, G. Mandaglio, M. Manganaro, and G. Giardina, *Phys. Rev. C* **81**, 034611 (2010).
- [58] A. K. Nasirov, G. Mandaglio, G. G. Giardina, A. Sobiczewski, and A. I. Muminov, *Phys. Rev. C* **84**, 044612 (2011).
- [59] Z. H. Liu and J. D. Bao, *Phys. Rev. C* **74**, 057602 (2006); **80**, 054608 (2009); **84**, 031602(R) (2011).
- [60] N. Wang, J. Tian, and W. Scheid, *Phys. Rev. C* **84**, 061601(R) (2011).
- [61] N. Wang, E. G. Zhao, W. Scheid, and S. G. Zhou, *Phys. Rev. C* **85**, 041601(R) (2012); N. Wang, E. G. Zhao, and W. Scheid, *ibid.* **89**, 037601 (2014).
- [62] L. Zhu, Z. Q. Feng, C. Li, and F. S. Zhang, *Phys. Rev. C* **90**, 014612 (2014); Z. Q. Feng, G. M. Jin, J. Q. Li, and W. Scheid, *ibid.* **76**, 044606 (2007).
- [63] A. S. Zubov, G. G. Adamian, N. V. Antonenko, S. P. Ivanova, and W. Scheid, *Phys. Rev. C* **68**, 014616 (2003).
- [64] G. G. Adamian, N. V. Antonenko, and W. Scheid, *Phys. Rev. C* **69**, 011601(R) (2004).
- [65] G. G. Adamian, N. V. Antonenko, and W. Scheid, *Phys. Rev. C* **69**, 014607 (2004).
- [66] G. G. Adamian, N. V. Antonenko, and W. Scheid, *Phys. Rev. C* **69**, 044601 (2004).
- [67] G. G. Adamian, N. V. Antonenko, W. Scheid, and A. S. Zubov, *Phys. Rev. C* **78**, 044605 (2008).
- [68] G. G. Adamian, N. V. Antonenko, and W. Scheid, *Eur. Phys. J. A* **41**, 235 (2009).
- [69] G. Adamian, N. Antonenko, and W. Scheid, Clustering effects within the dinuclear model, in *Clusters in Nuclei, Vol. 2*, Lecture Notes in Physics, Vol. 848, edited by C. Beck (Springer, Berlin, Heidelberg, 2012), pp. 165–227.
- [70] G. G. Adamian, N. V. Antonenko, and H. Lenske, *Nucl. Phys. A* **970**, 22 (2018).
- [71] J. W. Negele and D. Vautherin, *Phys. Rev. C* **5**, 1472 (1972).
- [72] J. C. Bernauer *et al.*, *Phys. Rev. C* **90**, 015206 (2014).
- [73] T. R. Gentile and C. B. Crawford, *Phys. Rev. C* **83**, 055203 (2011).
- [74] S. Liran, A. Marinov, and N. Zeldes, *Phys. Rev. C* **62**, 047301 (2000); **63**, 017302 (2000); **66**, 024303 (2002); [arXiv:nuc1th/0102055](https://arxiv.org/abs/nuc1th/0102055).
- [75] H. Koura, T. Tachibana, M. Uno, and M. Yamada, *Progr. Theor. Phys.* **113**, 305 (2005).
- [76] R. Smolańczuk, *Phys. Rev. C* **56**, 812 (1997).
- [77] V. Zagrebaev and W. Greiner, *Phys. Rev. C* **78**, 034610 (2008).
- [78] K. Siwek-Wilczynska, T. Cap, M. Kowal, A. Sobiczewski, and J. Wilczynski, *Phys. Rev. C* **86**, 014611 (2012); K. Siwek-Wilczynska, T. Cap, and M. Kowal, *ibid.* **99**, 054603 (2019).
- [79] K. P. Santhosh and V. Safoora, *Phys. Rev. C* **96**, 034610 (2017).